machines

MDPI

Article

A Hybrid Fractal-NURBS Model for Characterizing Material-Specific Mechanical Surface Contact

Leilei Zhang [1], Yingkun Mu [1], Kui Luo [1], Guang Ren [1] and Zisheng Wang [2,*]

[1] Department of Automation, Moutai Institute, Renhuai 564500, China; zhangleilei@mtxy.edu.cn (L.Z.); muyingkun@mtxy.edu.cn (Y.M.); luokui@mtxy.edu.cn (K.L.); renguang@mtxy.edu.cn (G.R.)
[2] Department of Industrial Engineering, Tsinghua University, Beijing 100084, China
* Correspondence: zisheng8@mail.tsinghua.edu.cn

Abstract

The reliability of mechanical systems hinges on analyzing the actual surface-to-surface contact area, which critically influences dynamic behavior, friction, material performance, and thermal dissipation. Uneven surfaces lead to incomplete contact, where only a fraction of asperities touch, creating a nominal contact area. This study proposes a novel fractal contact model for various mechanical behaviors between mechanical contact surfaces, integrating the Weierstrass–Mandelbrot fractal function and nonuniform rational B-spline interpolation (NURBS) to model material-dependent actual contact conditions. Furthermore, this research delved into the changes in thermal conductivity across the surfaces of metal materials within a simulated setting. It maintained a contact ratio ranging from 0.038% to 15.2%, a factor that remained unaffected by contact pressure. Both experimental and simulated findings unveiled an actual contact rate spanning from 0.44% to 1.06%, thereby underscoring the distinctive interface behaviors specific to different materials. The proposed approach provides fresh perspectives for investigating material–contact interactions and tackling associated engineering hurdles.

Keywords: mechanical surface; contact rate; finite element method; NURBS

Check for updates

Academic Editor: Ciro Santus

Received: 26 November 2025
Revised: 25 December 2025
Accepted: 29 December 2025
Published: 30 December 2025

Copyright: © 2025 by the authors. Licensee MDPI, Basel, Switzerland. This article is an open access article distributed under the terms and conditions of the Creative Commons Attribution (CC BY) license.

1. Introduction

Contact attributes between two uneven surface solids, including thermal contact resistance, assembly precision, electric switchers, etc., are crucial in engineering contact components. The characterization of the actual contact state of different contact surfaces is of great significance in solving the key technical problems in aviation, aerospace, shipbuilding, automobile, medical treatment, electronic packaging, and other industries [1–5]. However, the stochastic and intricate topographies of rough surfaces make evaluating the actual contact area challenging and hinder further investigation of macroscopic contact features.

The pioneering works of Bowden [6], Hertz [7], Archard [8,9], Greenwood et al. [10,11], Majumdar and Bhushan [12,13], Yan and Komvopoulos [14,15] have laid the foundation for prominent theories for exploring the properties of contact between uneven surfaces. These theories can be mainly divided into three categories: (i) single-scale multi-asperity contact model; (ii) truncation model; and (iii) multi-scale model. It is generally believed that the actual contact area between two metal surfaces depends on the plastic deformation of the contact surface and the highest microconvex body. Therefore, for a long time, researchers generally believed that the actual contact area between metal surfaces is proportional to the contact load. Archard [8,9] pointed out that plastic deformation could

not universal rule, and introduced a model that shows that the area of contact could be proportional to the load even with purely elastic contact. In contrast to earlier contact theories, Greenwood and Williamson [10] demonstrated how contact deformation relies on surface topography and formulated the criterion for differentiating between elastically and plastically touching surfaces, which is more related to a real contact situation. Majumdar and Bhushan [12,13] proposed a method of using fractal parameters to characterize planes with self-affine features, and developed a new model of contact between isotropic rough surfaces. According to the model, the relational expression for the real area of contact A_r and load P is $P \sim A_r^{(3-D)/2}$ in the case of elastic deformation, where D represents the surface profile's fractal dimension ranging between 1 and 2.

Yan and Komvopoulos [14,15] studied the relationship between elastic–plastic contact deformation and surface contact stiffness between three-dimensional fractal surfaces. In addition, they found that the real contact area is approximately one percent of the apparent contact area or less when the interfacial force is predominantly elastic. Yovanovich [16–19] has conducted extensive research on surface contact heat transfer, and its research results have achieved significant results in engineering applications such as nuclear, aerospace, and microelectronics in industries. Persson's [20–22] work on the contact between tires and roads led him to develop a potentially more widely used elastic contact theory, which involves the derivation and solution of the diffusion equation on the premise that there is no tension at the contact interface. The theory predicts that the area of contact in most cases varies linearly with the load. Thompson et al. [23] proposed a multi-scale iterative method when studying contact thermal resistance problems, which combines the measured surface geometry with the iterative thermal/structural finite element model to accurately predict micro and macro thermal contact resistance, quantitatively study the impact of manufacturing tolerances, and improve system performance. Leban et al. [24] found in their study on wheel–rail contact in railways that the nominal contact area exhibits a power–law relationship with load, whereas the elliptical Hertzian contact theory can only predict its average trend.

The aforesaid contact theory has greatly promoted the development of the theory of the qualitative description of interfacial contact attributes for uneven surfaces. In addition, the rapid development of computer technology has enabled researchers to use the powerful computational abilities of computers to analyze the contact behavior between surfaces. This led to valuable conclusions and aided the subsequent research works. A solution to the nonlinear interfacial contact problems of uneven surfaces is to numerically simulate rough contacts directly. Finite or boundary element methods are suitable for studying such problems [25–31]. Ta et al. [32] introduced a volumetric contact theory, which effectively explored electromechanical contact features between stochastic rough surfaces and could forecast the contact resistance variation with the squeezing load in the plastic and elastic zones. Yu et al. [33] put forward a thorough model of normal stiffness between bent fractal surfaces by considering the friction factor. Their work revealed that the contact stiffness displays nonmonotonic properties in addition to the trans-scale fluctuation of fractal roughness, which is reliant sensitively on the fractal dimension. Carvalho et al. [34] proposed a universal and valid multi-scale strategy, which furnishes how the rough contact modeling was achieved and the real contact area progression was identified. Compared to the analytical model, the computer-based finite and boundary element methods and finite volume methods are more flexible, allowing a large number of loose hypothesis sets and direct terrain analysis. Additionally, the real area of contact greatly impacts the stick-slip traits between the two contact materials [35–38]. Wang et al. [39] introduced a numerical model to explore the impact of surface roughness on the slipping and sticking of contacting surfaces made out of the same materials. The study revealed that a higher

root mean square (RMS) gradient for a fixed load results in a smaller contact area. Whereas when the RMS gradient was fixed, the impact of RMS roughness was negligible. Siddappa and Tariq [40] estimated the correlation between surface coarseness and contact area with thermal conductivity and compared different methods for estimating the surface topography parameters. They developed a semi-deterministic method to construct the actual surface topography. Guo et al. [41] investigated the static friction behavior of elastic–plastic spherical adhesive micro-contacts between a rigid flat and a deformable sphere under combined normal–tangential loading using the finite element method (FEM), and established an empirical dimensionless expression for the static friction coefficient that accounts for inter-molecular forces. Fukagai et al. [42] used an ultrasonic reflectometer to continuously monitor four train track interfaces with different initial morphologies. They studied the changes and relationships in the contact stiffness and friction coefficient as a function of repeated slip. A mechanical model of the contact interface was proposed based on the experimental results. The above methods have certainly promoted the development of surface contact behavior research in several aspects. However, the practical application of these models is restricted since estimating the real contact area between uneven surfaces is complicated.

This study focuses on the variation law of the thermal conductivity between metal contact surfaces for a contact ratio ranging between 0.038% and 15.2%. Actually, when the contact area exceeds 10%, the rate of increase in heat transfer becomes very slow as the contact area grows larger. Therefore, this paper only discusses cases where the contact area is within 15.2%. A comparison of the simulation results with the experimental results demonstrates that the real area of interfacial contact is between 0.44% and 1.06%. In a previous publication [1], we overestimated the inter-embedded portions of contacting bodies, resulting in analyzed actual contact areas that exceeded the true contact areas. This has been corrected in this study, and we believe the conclusions drawn here more accurately reflect the true contact area. It should be noted, however, that the present work was conducted based on the methodological framework established in prior research. The adopted method offers a novel perspective for studying various mechanical behaviors between mechanical contact surfaces and can provide insight to researchers in solving related engineering problems efficiently.

Figure 1 illustrates an outline of the research approaches employed in this work. To study the contact rate between metal planes, the surface topography characteristics of the research object were measured first, and the measured data were interpolated. A three-dimensional (3D) structure of the object was obtained using a mathematical method employing CATIA software (V5 version). Further, the contact area was set on a plane of the object to be studied. The contact pairs with a contact ratio between 0.038% and 15.2% were analyzed for heat transfer, and the elevation in temperature was estimated. Finally, the actual elevation in temperature for the studied contact joint was measured under the same conditions. In contrast, the real contact area for the studied object was determined through a comparison between simulated and experimental results. It is worth noting that the proposed research method avoids the mutual embedding of contact pairs, which makes the analysis result more reliable.

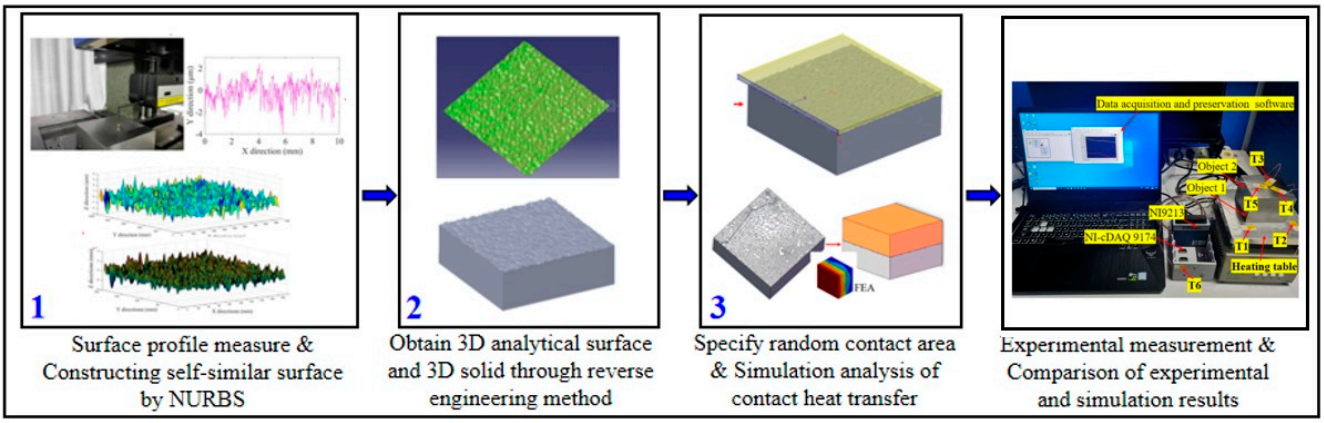


Figure 1. Overview of the research methods.

2. Surface Reconstruction Theory

Surface reconstruction draws extensive applications in the fields of data visualization, reverse engineering, virtual reality, machine vision, and medical technology. Considering the association of the reconstructed surface with the point cloud from data, the surface reconstruction approaches may be categorized as interpolation and approximation types. The reconstructed surface obtained by the interpolation approach entirely crosses the original data points. In contrast, the one obtained by the approximation approach approximates the original data points utilizing surface forms like a piecewise linear one. Thus, the local controllability of the nonuniform rational B-spline interpolation method enables the analysis of the reconstructed 3D surface using the finite element method. Hence, this study uses interpolation by a nonuniform global B-spline to reconstruct the point cloud data to ensure that the reconstructed surface features are similar to the 3D morphology of the real surface to the greatest extent.

2.1. NURBS Curve

For a nonuniform rational B-splines (NURBS) curve having a degree of p, its computational expression may be given as [43]

$$C(u) = \frac{\sum_{i=0}^{n} M_{i,p}(u)\omega_i P_i}{\sum_{i=0}^{n} M_{i,p}(u)\omega_i}, \; a \le u \le b \tag{1}$$

where P_i stands for the control point, ω_i denotes the weight coefficient corresponding to the control polygon vertex ($\omega_i \ge 0$). In no special circumstances, $a = 0$, b = 1, u is the transition parameter, and $M_{i,p}(u)$ refers to a pth B-spline basis function derivable by a node vector U based on the de Boor recursive formula. Its computational formula is given by [43]

$$M_{i,0}(u) =, \begin{cases} 1, u_i \le u \le u_{i+1} \\ 0, others \end{cases} \tag{2}$$

$$M_{i,p}(u) = \frac{u - u_i}{u_{i+p} - u_i} M_{i,p-1}(u) + \frac{u_{i+p+1} - u}{u_{i+p+1} - u_{i+1}} M_{i+1,p-1}(u) \tag{3}$$

The computational formula for node vector U is

$$U = \left\{ 0, \cdots, 0, u_{p+1,\cdots,u_{r-p-1}}, 1, \cdots, 1 \right\} \tag{4}$$

where $r = i + p + 1$, let [1]

$$R_{i,p}(u) = \frac{M_{i,p}(u)\omega_i}{\sum_{j=0}^{n} M_{j,p}(u)\omega_j} \tag{5}$$

Apart from being a rational basis function, $R_{i,p}(u)$ is also a piecewise rational function on u ϵ [0, 1]

$$C(u) = \sum_{i=0}^{n} R_{i,p}(u)P_i \tag{6}$$

where $R_{i,p}(u) = M_{i,p}(u)$ in case $\omega_i = 1$ for the entire i. The computational expression for the NURBS curve is

$$C(u) = \sum_{i=0}^{n} M_{i,p}(u)P_i \tag{7}$$

2.2. NURBS Surface

Analogous to splines, a NURBS surface having degrees of p and q separately along the U and V directions can be formulated to be a piecewise rational vector function as [43]

$$S(u,v) = \frac{\sum_{i=0}^{n}\sum_{j=0}^{m} M_{i,p}(u)M_{j,q}(v)\omega_{i,j}P_{i,j}}{\sum_{i=0}^{n}\sum_{j=0}^{m} M_{i,p}(u)M_{j,q}(v)\omega_{i,j}}, \qquad 0 \le u, v \le 1 \tag{8}$$

Similar to the parametric expression of a NURBS curve, in the above equation, $P_{i,j}$ represents the control point in (U, V) direction, $\omega_{i,j}$ stands for the weight coefficient, $M_{i,p}(u)$ and $M_{j,q}(v)$ refer to the spline basis functions defined separately in the node vectors' U and V directions. In addition, the computational formula for node vector V, which resembles that for U, is

$$V = \left\{0, \cdots, 0, u_{p+1,\cdots,u_{r-p-1}}, 1, \cdots, 1\right\} \tag{9}$$

where $s = m + p + 1$, let

$$R_{i,j}(u,v) = \frac{M_{i,p}(u)M_{j,q}(v)\omega_{i,j}}{\sum_{k=0}^{n}\sum_{l=0}^{m} M_{k,p}(u)M_{l,q}(v)\omega_{k,l}} \tag{10}$$

Thus, $R_{i,j}(u,v) = M_{i,p(u)}M_{j,q(v)}$ in case $\omega_{i,j} = 1$ for the entire i and j. The NURBS can be formulated as

$$S(u,v) = \sum_{i=0}^{n}\sum_{j=0}^{m} M_{i,p}(u)M_{j,q}(v)P_{i,j} \tag{11}$$

Appendix A for control point coordinates $\{P_{i,j}\}$ and node vector U and V. For detailed information on the interpolation process of discrete surfaces, one may refer to the previous articles published by our research team [44]. The non-uniform global B-spline interpolation method typically requires interpolation between given data points. If the spacing between data points is too large, it may lead to inaccurate interpolation results, as interpolation algorithms may not be able to fully capture subtle changes between data points. Therefore, when using this method for point cloud data reconstruction, it is necessary to fully consider the characteristics and requirements of the data and select appropriate interpolation functions and parameters to optimize the interpolation results.

In summary, the NURBS method has become one of the most important geometric modeling methods in curve and surface design systems. The steps of NURBS global interpolation usually involve the following key steps:

(1) Preparation stage

Clear interpolation objective: Determine the dataset that needs to be interpolated through NURBS curves, and perform necessary preprocessing on the shape points, such as denoising, smoothing, etc., to ensure the accuracy of the interpolation results.

(2) Parameterization stage

Choose parameterization method: Use an appropriate parameterization method to map the type value points onto the parameter field and obtain the corresponding parameter values. According to the parameterization method, construct node vectors and calculate the intermediate node values based on the parameterization method.

(3) Control vertex solving stage

Constructing interpolation equations: Based on the definition and properties of NURBS curves, construct interpolation equations for control vertices, and use numerical methods (such as iterative methods, matrix solving, etc.) to solve the interpolation equations to obtain a set of control vertices.

(4) Curve generation stage

Constructing NURBS curves: Using the obtained set of control vertices and node vectors U, construct NURBS curves that pass through shape points. Validate the generated NURBS curve and check if it meets the interpolation requirements. If necessary, adjust the control vertices or parameterization methods to optimize the interpolation results.

It should be noted that NURBS global interpolation is a complex process that involves multiple mathematical and computational problems. At the same time, the accuracy and reliability of interpolation results are also affected by various factors, such as the distribution of shape points, the selection of parameterization methods, and the accuracy of solving control vertices. Therefore, when performing NURBS global interpolation, it is necessary to comprehensively consider these factors to ensure the accuracy and reliability of the interpolation results.

3. Simulation and Experiment

The characteristics of the contact surface have a great impact on the normal operation of the mechanical equipment. However, due to the diversity and complexity of the processing technology, a very limited explicit theoretical basis is available in the literature for the contact surface. Previous research in surface-to-surface contact properties adopted the method of qualitative research, which uses complex formulae to describe the state of surface-to-surface contact. This often lacks intuition and is difficult for engineers to understand. Numerical simulation is a highly effective approach to exploring the thermal transfer phenomenon. Simulation of the whole thermal analysis process is achievable by setting identical thermal boundary conditions as an experimental context in the software, typified by temperature field visualization and short time expenditure. In this section, we will describe the real state of surface-to-surface contact using a 3D solid contact model of the contact surface and analyze the model using simulation.

3.1. Description of Finite Element Model

As shown in Figure 2, assuming that geometry #1 with a rough surface and fractal features is in contact with geometry #2 with a smooth surface, and then using the smooth surface to intercept some of the microconvex bodies of the rough surface, the processed contact pairs can be obtained. The effect after interception is shown in numbers 1 to 4 in the figure. When entities with rough surfaces come into contact with smooth entities, the actual surfaces that participate in the contact can be set as desired. As shown in the

figure *a* and *b*, only surface *a* participates in contact heat transfer. Therefore, as long as different contact rates are set and heat transfer analysis simulation tests are conducted, and compared with the experimental measurement results under the same conditions, the actual contact rate between two geometric bodies can definitely be determined. In addition, higher precision results can be obtained by setting smaller contact area increments. Finally, it is worth noting that the object #1 analyzed in this study is a common grinding surface in engineering. The three-dimensional geometric structure of the surface is obtained by measuring the morphology characteristics of the experimental geometry surface, combined with fractal functions and the NURBS global interpolation method [1].

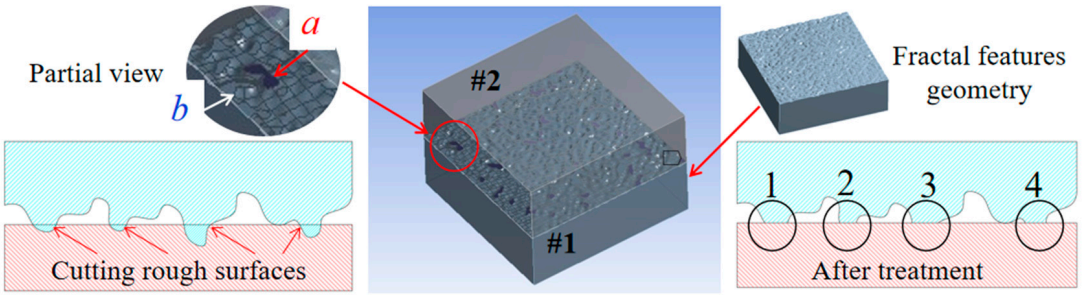


Figure 2. Simplification of the actual contact mode of the contact surface.

Figure 3a schematizes the contact model adopted for analyzing the thermal transfer traits of contact surfaces. The real contact area on surface B was set according to the research objective, and the thermal transfer between surfaces B and C was carried out through a small number of microconvex bodies. Figure 3b shows the heat transfer process between the B and C surfaces in Figure 2. The heat transfer across the interface may be either via solid conduction, where the bodies touch, or via interstitial heat transfer through the gaps. In cases where the contact surface is not smooth, the average temperature drop at the interface will be significantly greater than the temperature drop in the body.

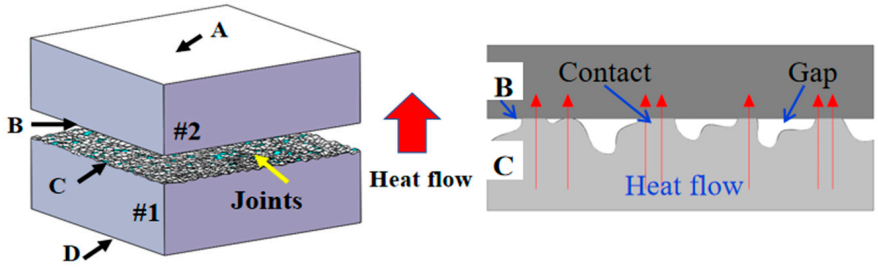


Figure 3. Thermal conduction mode between contact surfaces. (**a**) Contact model; (**b**) incomplete contact.

When two mechanical surfaces come into contact with each other, due to the high hardness and uneven surface morphology of the material, unlike the contact between rubber and metal surfaces, only a small number of microconvex bodies are in contact. When using the model in this research to analyze the actual contact area between contact surfaces, the contact area of the surfaces is known and visible. Another advantage of this model is that it can avoid analysis errors or even erroneous results caused by the mutual embedding of microconvex bodies when conducting planar contact heat transfer analysis, and it only focuses on determining the actual contact area between the contact surfaces.

3.2. Contact Characteristics of the Contact Model

It is well-known that the actual surface-to-surface contact area occupies only a small portion of the nominal contact area. However, earlier studies did not consider the size of the contact area. In a preliminary study, Yan and Komvopolous [14,15] introduced a comprehensive approach for assessing the contact mechanics of an uneven elastic–plastic surface. It featured a 3D fractal geometry and numerical outcomes that unravel the alterations of interfacial contact force and real contact area in the quasi-static surface stage. The interface force is primarily elastic for normal contact, and an inspected surface interference range of the ideal elastic–plastic silica surface. However, the real contact area is smaller than the apparent area of contact, or is about 1% or even lower, depending on the mean interfacial distance. However, it is challenging to determine the distance between the contact surfaces in engineering scenarios. The analysis involves various uncertain factors and requires a deep mathematical foundation, which is sometimes inconvenient but holds high academic significance concurrently.

Due to the complexity of the actual contact situation between the contact surfaces, some assumptions were inevitably made when using the finite element method to analyze the actual contact rate of the contact pairs in this study:

1. The pressure between the contact surfaces is constant.
2. Thermal radiation is ignored.
3. Do not consider the thermal convection in the gap.
4. Assuming that all materials in the finite element model exhibit linear elastic behavior and have no temperature dependence. No thermal expansion is allowed, and no coefficient of thermal expansion is defined.

In order to examine the real area of contact between two mechanical surfaces, contact surfaces (a)~(q), respectively, were chosen, as shown in Figure 4. The actual contact area was within the range of 2.1–854.3 mm^2. The contact point has been marked green in the figure. This setting can help to more accurately study the relationship between actual contact area and nominal contact area, avoiding interference caused by mutual embedding between contact surfaces. The contact rate was between 0.038% and 15.2%. It is evident from the figures that the position of the contact points is randomly distributed and is closer to the real contact conditions of actual contact surfaces.

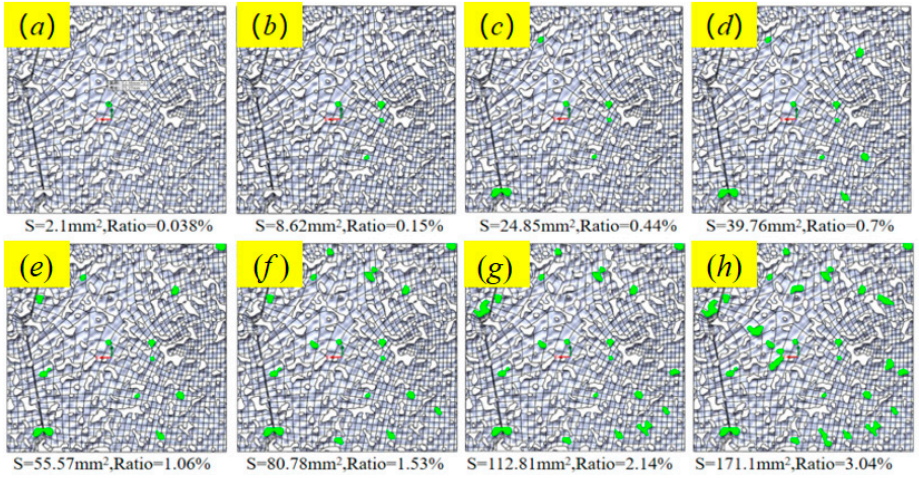


Figure 4. *Cont.*

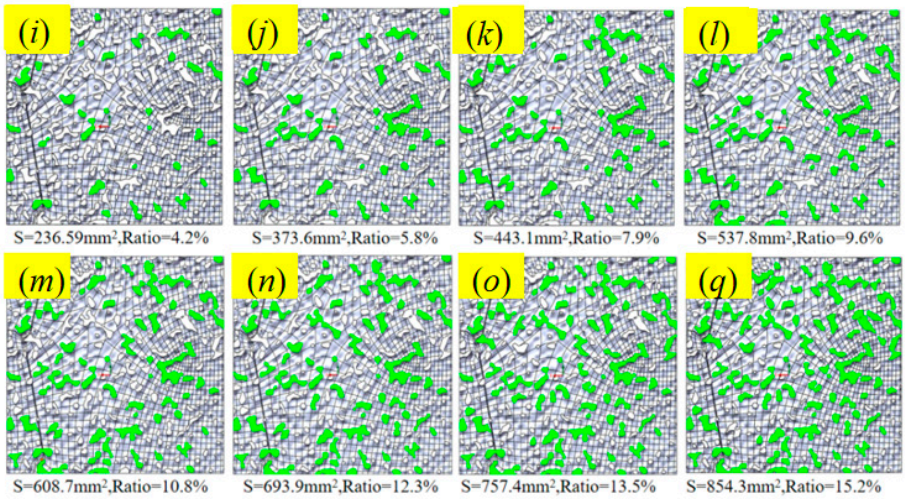


Figure 4. Real contact rate setting of contact surface.

3.3. Simulation

The contact model used in the proposed work, as well as the previous research work completed by our research team, is in millimeter scale. However, the real roughness of the contact surface is usually in the micrometer scale. There are two main reasons for avoiding the micrometer scale in the simulation. Primarily, analysis in a microscale grid utilizes a considerable amount of computer memory, affecting the calculation efficiency. This may make the calculations very difficult or even impossible to complete. Secondly, as the micrometer and millimeter scales are very small compared to the intrinsic metal block thickness, when the heat transfer process from Surface D through Surfaces C and B to Surface A, the thermal conduction within the metal block itself plays a dominant role. This is one of the complications that has been paid attention to in this study. After determining the contact area and formulating the thermal boundary conditions, the thermal transfer process of the mechanical contact pairs under different contact rates was simulated in the ANSYS (19.0 version) simulation environment. Table 1 details the thermal boundary conditions in the simulation environment. Surface A mainly interacts with ambient air by natural convection, and its heat transfer coefficient h = 9.7 W/m^2 K is provided by [45]. The same applies to the sides of the two geometric bodies. Obviously, there is no air flow on surfaces B, C, and D, and the convective heat transfer coefficient is 0. In addition, the initial temperature load is added on surface D, where the temperatures of surfaces B and C are 0, and the temperature of surface D is 100 °C. The ambient temperature is consistent with the experiment ambient temperature, which is 27.5 °C. The contact bodies #1 and #2 are made from structural steel (E = 200 GPa, v = 0.25, k = 60.5 Wm^{-1} K^{-1}). All materials in the finite element models are assumed to demonstrate linear elastic behavior and assumed to have no temperature dependence. Thermal expansion was not permitted, and no thermal expansion coefficient was defined. For this research, which was conducted at room temperature, thermal conduction and convection are the dominant heat transfer mechanisms across the gaps, thermal radiation is negligible, and quantum effects can be ignored even at relatively small length scales, so the assumptions made are reasonably valid. If higher model temperatures (>300 °C) were required, thermal radiation should be added.

Table 1. Thermal boundary conditions (T = 100 °C).

Object Surface	CHTCs (W/m^2 K)	Temperature (°C)	Ambient (°C)
A	9.7	0	27.5
B	0	0	27.5
C	0	0	27.5
D	0	100	27.5

After determining the corresponding thermal boundary conditions, we can analyze the heat transfer characteristics of the contact model at different contact rates. Figure 5 depicts the temperature field of the contact model's surface A. The contact rate variations range from 0.038% to 3.04%. It shows the temperature field distribution of surface A under different contact rates in a balanced heat state. The research results in the figure are obvious: the maximum temperature of surface A increases from 62.7 °C to 97.32 °C. It is understood that the actual contact rate of the contact surface greatly affects the heat transfer between the contact surfaces. In addition, from the analysis results, it can be seen that the temperature on surface A is not uniformly distributed, and the high-temperature area is mainly concentrated in the geometric center of surface A. Therefore, when using experimental methods to measure the temperature of surface A, it is necessary to set up as many temperature collection points as possible to collect the average temperature, in order to reduce the control error.

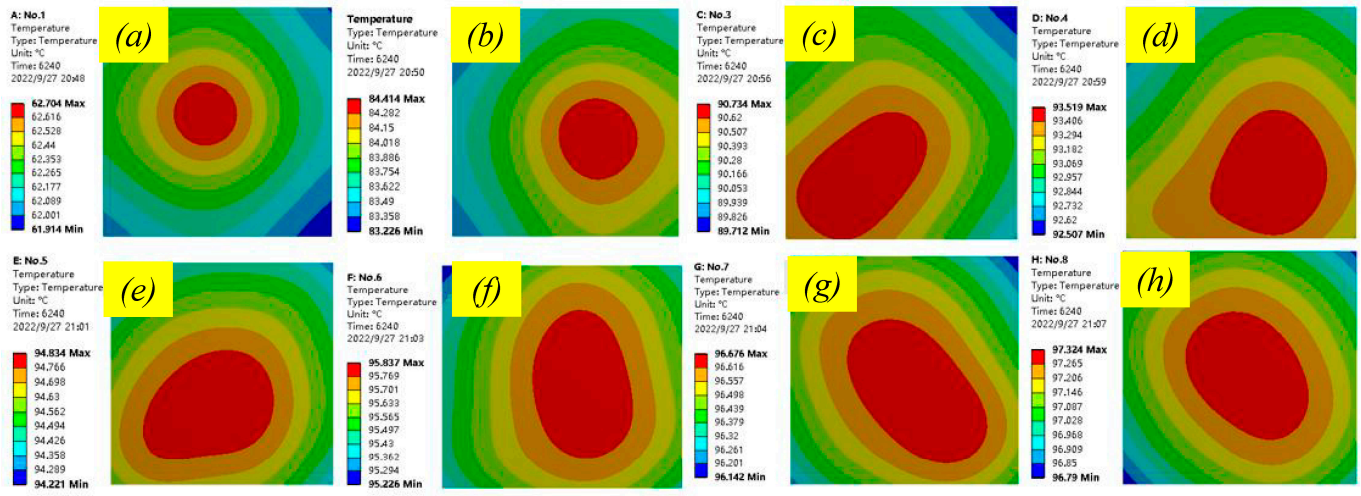


Figure 5. The temperature field of surface A. (**a**) Ratio = 0.038%, (**b**) Ratio = 0.15%, (**c**) Ratio = 0.44%, (**d**) Ratio = 0.7%, (**e**) Ratio = 1.06%, (**f**) Ratio = 1.53%, (**g**) Ratio = 2.14%, (**h**) Ratio = 3.04%.

The simulation results reveal that the metal exhibits excellent thermal conductivity, its thermal resistance is less, and the incomplete contact between the contact surfaces is the key factor hindering the heat transfer between the contact surfaces. The incomplete impact of the mechanical joint influences the equilibrium of heat conduction between the contact surfaces, which is of great importance in various engineering analyses, including the real-time compensation of the thermal error of the machine tool [5]. The proposed work focuses on the contact heat transfer experiment of the slider to eliminate the delay impact of the incomplete contact of the mechanical joint on the heat conduction time. The main reason for the thermal delay is the contact thermal resistance caused by incomplete contact of the mechanical contact surface. For the contact thermal resistance between metal surfaces, Thompson [23] proposed another method for studying the contact thermal resistance of metal surfaces. By measuring the micro morphology of the studied surface and analyzing the contact behavior between metal surfaces at the micro scale, Thompson solved the contact

thermal resistance between metal surfaces using iterative methods. For the imported surface model, her proposed method predicted a good match between the macro-scale contact mode and the experimental contact mode, which has been experimentally validated.

4. Results

Experiments were conducted on the simulation objects to validate the simulation results and identify the actual contact area between the plates. The layout of this experiment is shown in Figure 12 of [1]. The instruments involved in the experiments included heating tables, thermocouple temperature sensors, NI-cDAQ 9174 data acquisition systems, NI9123 data acquisition cards, and computers. The heat transfer experiment between the plates followed the compilation of the data acquisition program. In order to better compare the experimental results with the simulation results, thermocouple temperature sensors T3, T4, and T5 are connected, and the average temperature of the three points is taken as the reference value of the measured surface temperature. The sampling frequency is set to 1 Hz, which means recording temperature data every second. The collection program is written through LabVIEW software (2020 version), which can save the collected temperature data in. txt format, and then use MATLAB (2022a version) to plot and compare the collected data for analysis. It is worth noting that before placing a flat plate on the heating table for experimental data collection, it is necessary to observe whether the values of thermocouple sensors T1 and T2 are stable at 100 °C. Due to the high thermal conductivity of metals and their sensitivity to the experimental environment, even small changes in the experimental environment can directly affect the reliability of measurement results. Therefore, it is necessary to minimize the uncertainty introduced by environmental factors as much as possible, and the temperature change in the measurement environment should not exceed 1 °C. The pink line segment displayed in Figure 6 represents the average temperature rise in the upper surface of the flat plate in the measurement process, which is measured by the temperature sensors T3, T4, and T5. The ambient temperature is recorded by the thermocouple temperature sensor T6, and the temperature rise process is shown in the bottom pink curve in Figure 6. It can be seen that the ambient temperature is basically stable at around 27.5 °C, which is consistent with the ambient temperature set in the previous analysis.

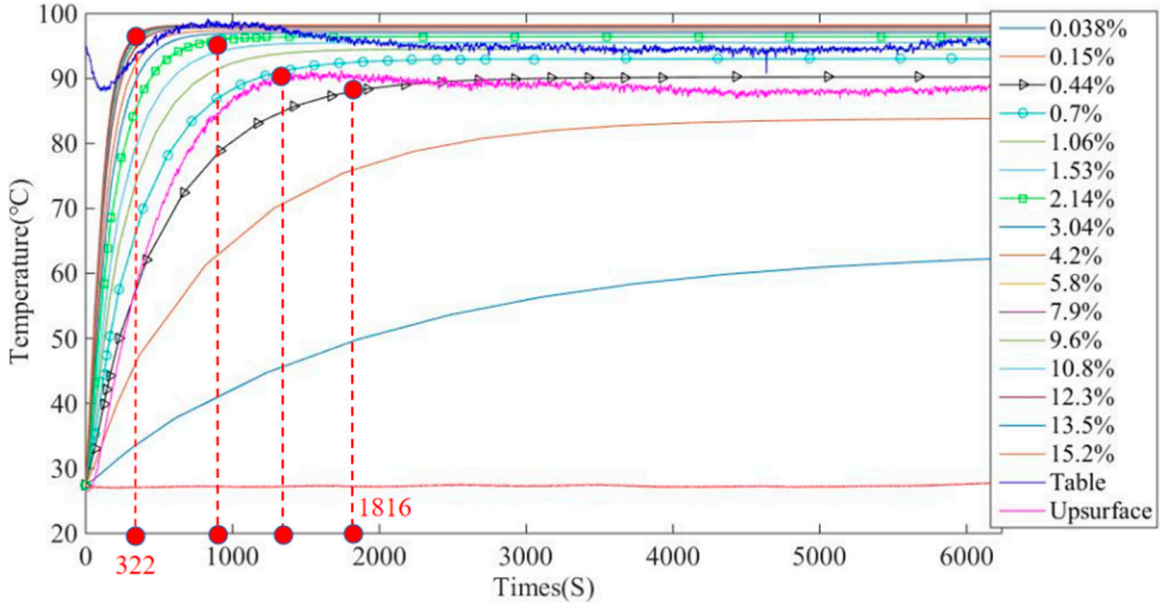


Figure 6. Comparison of temperature variations in surface A between experimental and simulation methods.

The blue curve stands for the average temperature variation in the heating table in the measurement process, and the average temperature is measured by sensors T1 and T2. The blue curve here first decreases and then rises. It is due to the large temperature difference between the heating table and the metal objects during the initial heating of the metal geometry in the experiment. After the temperature of the metal block rises, the temperature of the heating table tends to stabilize. But the measured surface temperature is slightly lower than 100, which is caused by surface heat dissipation. However, there is no convective heat dissipation on the surface of the contact area between the countertop and the metal object 1, and the temperature of the countertop in this area is 100 °C. The other curves represent the average temperature changes in the slider surface A during the entire process of the slider contact rate changing from 0.038% to 15.2% in the simulation environment. Figure 7 shows that the measured and simulated values of actual temperature rise in the upper surface A of the plate are close, equal to 0.44% and 0.7%, respectively. Thus, it may be concluded that the actual contact area between the two sliders is between 0.44% and 0.7%. These comparison results affect the temperature field distribution characteristics of the system under the thermal balance state. Additionally, it reveals that with the increase in the indirect contact rate of the slider, the time required for the heat transfer system to reach the thermal balance shortens rapidly. The system attains thermal balance within 1816 s, when the contact rate is equal to 0.44%, whereas it achieves thermal balance in 322 s when the contact rate is greater than 2.14%.

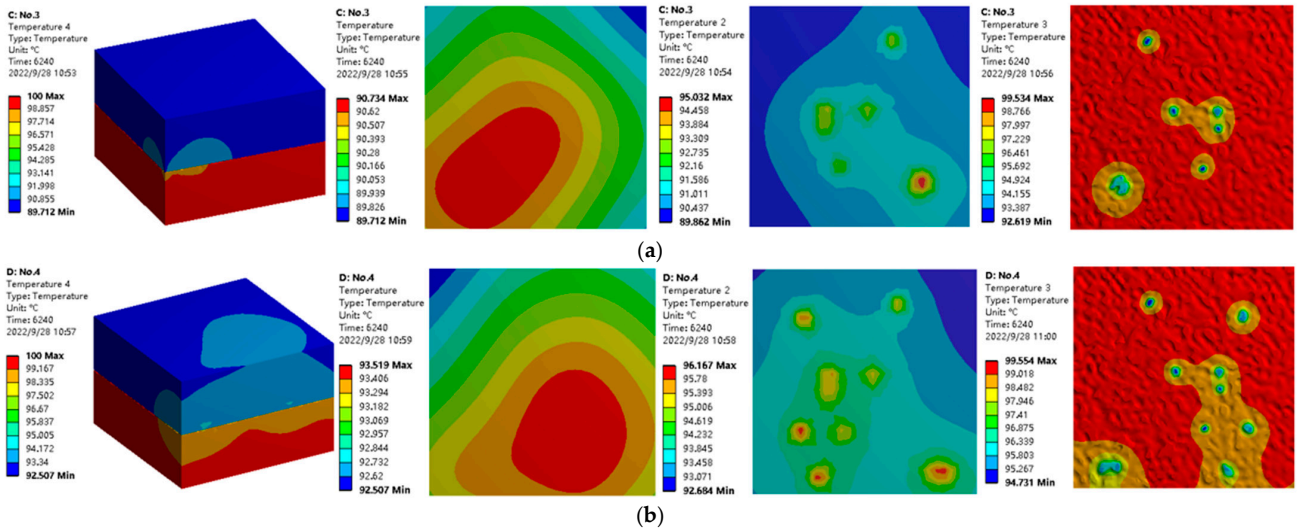


Figure 7. Temperature field distribution characteristics of sliding block under different contact rates. (**a**) Contact rate is 0.44%; (**b**) contact rate is 0.7%.

The heat transfer between the sliders was measured under different boundary conditions, and the obtained results were compared with simulation results to validate the proposed concept. The new thermal boundary conditions are furnished in Table 2. The results obtained in the proposed study are more convincing as it avoids contact pairs normally present in previous studies.

Table 2. Thermal boundary conditions (T = 51.5 °C).

Object Surface	CHTCs (W/m^2 K)	Power (°C)	Ambient (°C)
A	9.7	0	27.5
B	0	0	27.5
C	0	0	27.5
D	0	51.5	27.5

The pink-colored curve in Figure 8 represents the increase in temperature on the upper surface of the slider. The measured value of the temperature of the heating table is 51.5 °C, which is the average temperature of the temperature sensors T3, T4, and T5. The other curves represent the average temperature rise in the upper surface of the slider measured in the simulation environment at different contact rates. The bottom red curve records the temperature rise in the environment recorded by the sensor T7. It can be seen from the results that the ambient temperature is stable at 27.5 °C during the measurement process. Further, the temperature rise in the upper surface includes two plates with a contact ratio of 0.44% and 1.06%, which is very close to the temperature rise curve with a contact ratio of 0.7%. It may be inferred that the actual contact rate between the contact surfaces is between 0.44% and 1.06%, approximately 0.7%. This finding is consistent with the measured result when the temperature of the heating table is 100 °C. It can also be inferred that the actual contact area between the sliding blocks is approximately 0.7%, which is less than 1%. This finding is consistent with the research of Yan and Komvopolous' model [14]. However, the method introduced in this article avoided the complex mathematical extrapolation process, as introduced in Section 3.2. Even researchers without a deep mathematical foundation can understand, which is a characteristic of this method.

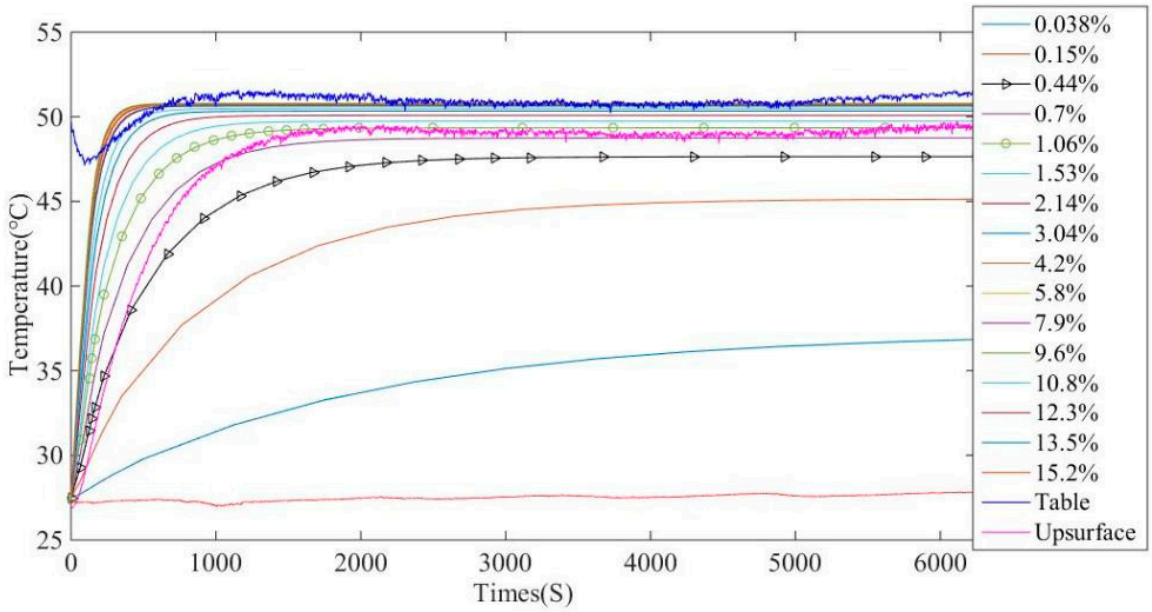


Figure 8. Comparison of simulation and experiment results.

Figure 9 presents the temperature field distribution of the sliding block at a contact rate of 0.44% and 1.06%. From the figure, it may be observed that a small number of contact pairs result in a significant temperature difference on the contact boundary of the two sliding blocks, which is caused by the heat transfer between the sliding blocks. A contact ratio of 0.44% results in a temperature settlement of the contact surface of approximately 1.43 °C, and a contact ratio of 1.06% results in a temperature settlement of the contact surface of approximately 0.79 °C, as shown in Figure 9a and Figure 9b, respectively. It can be inferred that an increase in temperature escalates the temperature difference caused by incomplete contact between the contact surfaces. Hence, it is essential to consider the incomplete contact between the contact surfaces while analyzing problems involving high-temperature contact heat transfer. Otherwise, the analysis will lead to distorted results.

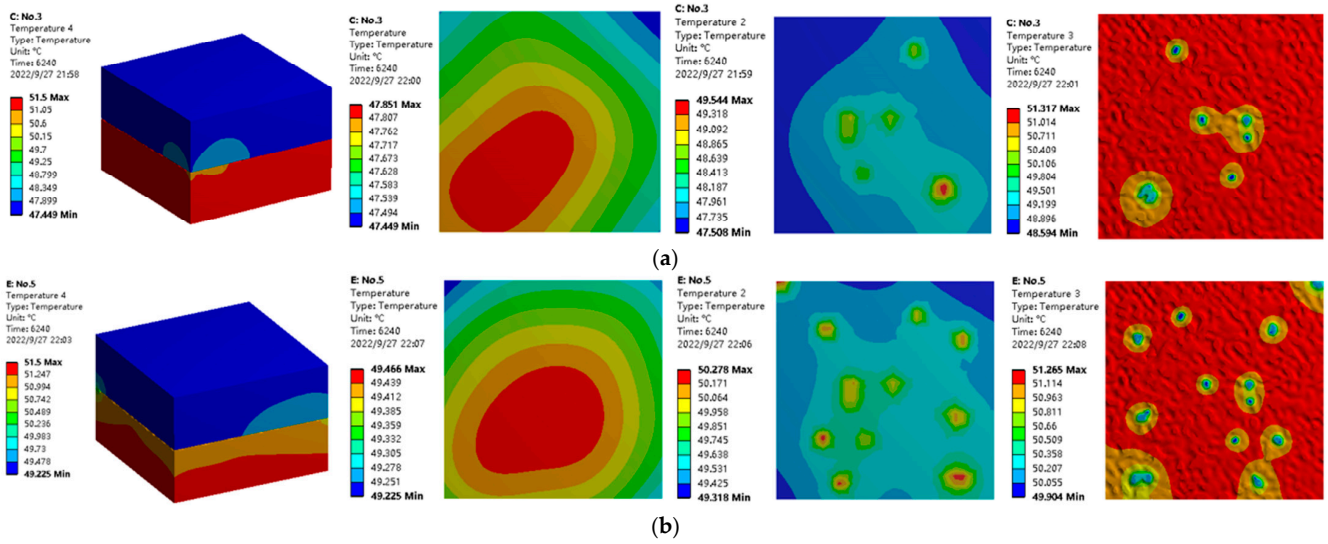


Figure 9. Temperature field distribution characteristics of sliding block under different contact rates. (**a**) Contact rate is 0.44%; (**b**) contact rate is 1.06%.

It may be noted that the obtained simulation results do not conform well to the experimental results. This may be because the simulation involves solving partial differential equations, which is a test of the corresponding process of partial differential equations. Moreover, the simulation model has been simplified to a certain extent, which must have added to the inconsistency between the simulated and measured results. However, the comparative analysis clearly shows that the simulated temperature field in this study satisfactorily explains the temperature rise measured in the experiment. Additionally, this study reveals an intuitive way of real contact state between the contact surfaces, which can be used as a reference for researchers in the fields of CPU cooling mode, machine tool thermal error compensation, etc.

5. Discussion

The previous literature on planar contact has predominantly concentrated on the modeling and analysis of microscopic contact states, typically adopting a theoretical framework wherein the contact process is assumed to progress sequentially through three distinct stages: elastic deformation, elastoplastic transition, and fully plastic deformation. Within this conventional paradigm, researchers have extensively discussed the characteristic contact scale corresponding to each stage as a means to estimate the true contact area between rough surfaces. However, a notable limitation of such approaches is the inherent separation between microscopic-scale interactions and macroscopic-scale mechanical behavior, creating a conceptual and methodological gap that complicates direct experimental validation of the proposed theoretical models. This persistent challenge arises from the difficulty in simultaneously observing and quantifying phenomena across vastly different length scales using conventional experimental techniques. The methodology introduced in the present study addresses this longstanding issue by employing an integrated simulation-experimental strategy to systematically investigate the actual contact area of engineering surfaces. Through this dual approach, we have successfully bridged the traditional divide between micro- and macro-scale contact phenomena, establishing a unified framework for characterizing the contact behavior of rough surfaces across multiple scales. While the specific techniques employed in this investigation may generate some academic discussion regarding their underlying assumptions, the strong correlation observed between laboratory measurements and computational predictions provides compelling evidence

supporting the practical utility and reference value of our findings. It is crucial to emphasize that the contact analysis model implemented in this research represents a purposeful simplification of the actual geometric and morphological complexity inherent to real-world contact surfaces; consequently, the model possesses inherent limitations that must be acknowledged. Several important aspects remain unexplored in the current work and warrant focused attention in future investigations. These include, but are not limited to the following: the nonlinear thermal expansion behavior of materials under varying temperature regimes, the dynamic relationship between actual contact ratio and applied load under changing surface pressure conditions, heat transfer mechanisms across contacting interfaces in the presence of lubricating media, the influence of surface adhesion and molecular adsorption effects on contact mechanics, as well as the role of subsurface cracks and material flaws in altering contact stress distributions and deformation patterns. Each of these factors represents a significant avenue for extending and refining the current understanding of planar contact phenomena.

Future work will build an integrated "geometry-material-mechanism-data" process based on the proposed hybrid fractal-NURBS contact framework. First, we will combine the model with adaptive knowledge transfer based on a large language model to enable online reasoning and interpretation across materials and conditions for contact-driven reliability analysis and diagnosis [46]. Second, we will embed adaptive domain reinforcement features and adversarial reinforcement learning to achieve robust generalization of morphological contact indices (e.g., actual contact rate and heat flow path) under distribution shifts [47,48]. Third, we will explore spiking neural networks with continuous time–frequency gradients to capture sparse transient thermodynamic events and multi-scale roughness activations, thereby improving sensitivity in the ultra-low contact rate range (0.44–1.06%) [49]. Finally, we will develop physically constrained neural network operators with uncertainty quantification to support real-time digital twins and in-service monitoring, enabling end-to-end prediction and closed-loop optimization from surface morphology to contact behavior and system performance [46–49].

6. Conclusions

This research work proposes a method that offers a new perspective for studying various mechanical behaviors between mechanical contact surfaces. The study is based on heat transfer theory, the finite element method, and NURBS global interpolation technology. The analysis performed through simulation is validated using experimental results, and obtained some beneficial conclusions:

(1) The results demonstrate that the actual contact area between contact surfaces is much less compared to its nominal contact area, accounting for only 0.44% to 1.06% of its nominal contact area.
(2) It is feasible to use macroscopic laboratory analysis to analyze the contact characteristics under a microscopic contact state.
(3) The incomplete contact between surfaces will cause obvious temperature settlement between the contact surfaces. Moreover, the delay in heat transfer affects the thermal equilibrium, thereby causing difficulty in analyzing thermal problems.

Author Contributions: Conceptualization, L.Z. and Z.W.; Methodology, L.Z.; Validation, Y.M., K.L. and Z.W.; Formal analysis, L.Z., Y.M., K.L., G.R. and Z.W.; Writing—original draft, L.Z. and Y.M.; Writing—review & editing, L.Z., K.L., G.R. and Z.W.; Visualization, L.Z.; Supervision, Z.W.; Funding acquisition, L.Z. All authors have read and agreed to the published version of the manuscript.

Funding: This research was financially supported by the Moutai High level talent project (grant nos. mygccrc [2022] 106, mygccrc [2022] 109, mygccrc [2022] 111, mygccrc [2022] 115, KY [2020] 223, and KY [2023] 119).

Data Availability Statement: The data presented in this study are available on request from the corresponding author.

Conflicts of Interest: The authors declare no conflicts of interest.

Appendix A

$$\mathrm{P}(:,:,1) = \begin{bmatrix} 0.200 & 2.137 & 7.674 & \cdots & 196.20 \\ 0.200 & 2.137 & 7.674 & & 196.20 \\ & \vdots & & \ddots & \vdots \\ 0.200 & 2.137 & 7.674 & \cdots & 196.20 \\ 0.200 & 2.137 & 7.674 & \cdots & 196.20 \end{bmatrix}_{50\times 50}$$

$$\mathrm{P}(:,:,2) = \begin{bmatrix} 0.200 & 0.200 & 0.200 & \cdots & 0.200 \\ 2.736 & 2.736 & 2.736 & & 2.736 \\ & \vdots & & \ddots & \vdots \\ 193.27 & 193.27 & 193.27 & \cdots & 193.27 \\ 196.20 & 196.20 & 196.20 & & 196.20 \end{bmatrix}_{50\times 50}$$

$$\mathrm{P}(:,:,3) = \begin{bmatrix} 1.149 & -10.637 & 12.791 & \cdots & -8.769 \\ -15.420 & 32.809 & -4.901 & & -1.417 \\ & \vdots & & \ddots & \vdots \\ 31.688 & 17.590 & 9.633 & \cdots & -22.700 \\ 3.317 & -4.190 & -20.770 & & -5.823 \end{bmatrix}_{50\times 50}$$

$$\mathrm{U} = [0 \quad 0 \quad 0 \quad 0.0382 \quad 0.0586 \quad 0.0790 \quad \cdots \quad 0.9032 \quad 1 \quad 1 \quad 1 \quad 1]_{1\times 54}$$

$$\mathrm{U} = [0 \quad 0 \quad 0 \quad 0.0375 \quad 0.0568 \quad 0.0786 \quad \cdots \quad 0.9579 \quad 1 \quad 1 \quad 1 \quad 1]_{1\times 54}$$

References

1. Zhang, L.; Yuan, J.; He, S.; Huang, S.; Xiong, S.; Shi, T.; Xuan, J. Contact heat transfer analysis between mechanical surfaces based on reverse engineering and FEM. *Tribol. Int.* **2021**, *161*, 107097. [CrossRef]
2. Wang, Z.; Xuan, J.; Shi, T. An autonomous recognition framework based on reinforced adversarial open set algorithm for compound fault of mechanical equipment. *Mech. Syst. Signal Process.* **2024**, *219*, 111596. [CrossRef]
3. Wang, Z.; Xuan, J.; Shi, T. Multi-source information fusion deep self-attention reinforcement learning framework for multi-label compound fault recognition. *Mech. Mach. Theory* **2023**, *179*, 105090. [CrossRef]
4. Liang, X.-M.; Chen, S.-W.; Li, C.-Y.; Niu, X.; Wang, G.-F. A general contact model for rough surfaces based on the incremental concept. *Tribol. Int.* **2024**, *198*, 109882. [CrossRef]
5. Weng, L.; Kizaki, T.; Ma, C.; Gao, W.; Kono, D. A review of robust thermal error reduction of machine tools. *Int. J. Mach. Tools Manuf.* **2025**, *209*, 104298. [CrossRef]
6. Bowden, F.; Tabor, D. *The Friction and Lubrication of Solids*; Part I, Clarendon; Oxford Academic: Oxford, UK, 1950.
7. Hertz, H. On the contact of elastic solids. *J. Reine Angew. Math.* **1882**, *92*, 156–171. [CrossRef]
8. Archard, J.F. Contact and rubbing of flat surfaces. *J. Appl. Phys.* **1953**, *24*, 981–988. [CrossRef]
9. Archard, J.F. Elastic deformation and the laws of friction. *Proc. R. Soc. Lond. Ser. A Math. Phys. Sci.* **1957**, *243*, 190–205. [CrossRef]
10. Greenwood, J.A.; Williamson, J.B.P. Contact of nominally flat surfaces. *Proc. R. Soc. Lond. Ser. A Math. Phys. Sci.* **1966**, *295*, 300–319. [CrossRef]
11. Greenwood, J.A. The Area of Contact Between Rough Surfaces and Flats. *J. Lubr. Technol.* **1967**, *89*, 81–91. [CrossRef]
12. Majumdar, A.; Bhushan, B. Fractal model of elastic-plastic contact between rough surfaces. *J. Tribol.* **1991**, *113*, 1–11. [CrossRef]

13. Majumdar, A.; Bhushan, B. Role of fractal geometry in roughness characterization and contact mechanics of surfaces. *J. Tribol.* **1990**, *112*, 205–216. [CrossRef]
14. Komvopoulos, K.; Yan, W. Three-Dimensional Elastic-Plastic Fractal Analysis of Surface Adhesion in Microelectromechanical Systems. *J. Tribol.* **1998**, *120*, 808–813. [CrossRef]
15. Yan, W.; Komvopoulos, K. Contact analysis of elastic-plastic fractal surfaces. *J. Appl. Phys.* **1998**, *84*, 3617–3624. [CrossRef]
16. Yovanovich, M.M. Overall constriction resistance between contacting rough wavy surfaces. *Int. J. Heat Mass Transf.* **1969**, *12*, 1517–1520. [CrossRef]
17. Fenech, H.; Yovanovich, M.M. Thermal contact conductance of nominally flat rough surfaces in a vacuum environment. In *Thermophysics and Temperature Control of Spacecraft and Entry Vehicles*; Heller, G.B., Ed.; Academic Press: New York, NY, USA, 1966; Volume 18, pp. 773–794.
18. Yovanovich, M.M. Thermal-mechanical models for non-conforming surface contacts. In Proceedings of the ITHERM 2000. The 7th Intersociety Conference on Thermal and Thermomechanical Phenomena in Electronic Systems, Las Vegas, NV, USA, 23–26 May 2000; Volume I.
19. Merevis, V.; Margaronis, K.; Papadopoulos, V. Thermomechanical analysis of the effect of contact forces in heat conduction of composite materials through multiscale contact finite element modeling. *Mech. Adv. Mater. Struct.* **2023**, *30*, 3365–3384. [CrossRef]
20. Persson, N.J. Theory of rubber friction contact mechanics. *J. Chem. Phys.* **2001**, *115*, 3840–3861. [CrossRef]
21. Persson, B.N.J.; Bucher, F.; Chiaia, B. Elastic contact between randomly rough surfaces: Comparison of theory with numerical results. *Phys. Rev. B* **2002**, *65*, 184106. [CrossRef]
22. Persson, B.N.J. Adhesion between an elastic body and a randomly rough hard surface. *Eur. Phys. J. E* **2002**, *8*, 385–401. [CrossRef] [PubMed]
23. Thompson, M.K. A Multi-Scale Iterative Approach for Finite Element Modeling of Thermal Contact Resistance. Ph.D. Thesis, Massachusetts Institute of Technology, Cambridge, MA, USA, 2007.
24. Leban, B.; Russo, M.; Freudenberger, M.; Trausmuth, A.; Varga, M.; Vernes, A. Applicability of an Hertzian-type contact model for wheel-rail pairings as seen by an improved post-processing scheme for ultrasonic data. *Tribol. Int.* **2024**, *195*, 109593. [CrossRef]
25. Manners, W.; Greenwood, J.A. Some observations on persson's diffusion theory of elastic contact. *Wear* **2006**, *261*, 600–610. [CrossRef]
26. Wang, L.; Tang, Q.; Liang, T.; Liu, C.; Sun, D.; Wang, S.; Li, J.; Zhang, S.; Meng, Y.; Huang, Y. Lubrication performance of graphene in the sliding electrical contact interface. *Friction* **2024**, *12*, 2760–2773. [CrossRef]
27. Pei, L.; Hyun, S.; Molinari, J.F.; Robbins, M.O. Finite element modeling of elasto-plastic contact between rough surfaces. *J. Mech. Phys. Solids* **2005**, *53*, 2385–2409. [CrossRef]
28. Hyun, S.; Robbins, M.O. Elastic contact between rough surfaces: Effect of roughness at large and small wavelengths. *Tribol. Int.* **2007**, *40*, 1413–1422. [CrossRef]
29. Campañá, C. Using Green's function molecular dynamics to rationalize the success of asperity models when describing the contact between self-affine surfaces. *Phys. Rev. E* **2008**, *78*, 026110. [CrossRef]
30. Goryacheva, I.G.; Dobychin, M.N. Multiple contact model in the problems of tribomechanics. *Tribol. Int.* **1991**, *24*, 29–35. [CrossRef]
31. Paggi, M.; Ciavarella, M. The coefficient of proportionality κ between real contact area and load, with new asperity models. *Wear* **2010**, *268*, 1020–1029. [CrossRef]
32. Ta, W.; Qiu, S.; Wang, Y.; Yuan, J.; Gao, Y.; Zhou, Y. Volumetric contact theory to electrical contact between random rough surfaces. *Tribol. Int.* **2021**, *160*, 107007. [CrossRef]
33. Yu, X.; Sun, Y.; Zhao, D.; Wu, S. A revised contact stiffness model of rough curved surfaces based on the length scale. *Tribol. Int.* **2021**, *164*, 107206. [CrossRef]
34. Carvalho, R.P.; Carneiro, A.M.C.; Pires, F.M.A.; Doca, T. An efficient multiscale strategy to predict the evolution of the real contact area between rough surfaces. *Tribol. Int.* **2021**, *165*, 107255. [CrossRef]
35. Hyun, S.; Pei, L.; Molinari, J.F.; Robbins, M.O. Finite-element analysis of contact between elastic self-affine surfaces. *Phys. Rev. E* **2004**, *70*, 026117. [CrossRef] [PubMed]
36. Zhao, J.; Wang, Z.; Zhengminqing, L.; Zhu, R. Fractal simulation of surface topography and prediction of its lubrication characteristics. *Surf. Topogr. Metrol. Prop.* **2021**, *9*, 045038. [CrossRef]
37. Carneiro, A.M.C.; Carvalho, R.P.; Pires, F.M.A. Representative contact element size determination for micromechanical contact analysis of self-affine topographies. *Int. J. Solids Struct.* **2020**, *206*, 262–281. [CrossRef]
38. Temizer, I. Thermomechanical contact homogenization with random rough surfaces and microscopic contact resistance. *Tribol. Int.* **2011**, *44*, 114–124. [CrossRef]
39. Wang, D.; Boer, G.D.; Neville, A.; Ghanbarzadeh, A. A new numerical model for investigating the effect of surface roughness on the stick and slip of contacting surfaces with identical materials. *Tribol. Int.* **2021**, *159*, 106947. [CrossRef]
40. Siddappa, P.G.; Tariq, A. Contact area and thermal conductance estimation based on the actual surface roughness measurement. *Tribol. Int.* **2020**, *148*, 106358. [CrossRef]

41. Xiang, G.; Goltsberg, R.; Etsion, I. Modeling static friction behavior of elastic–plastic spherical adhesive microcontact in full-stick condition. *Friction* **2024**, *12*, 2594–2610. [CrossRef]
42. Fukagai, S.; Marshall, M.B.; Lewis, R. Transition of the friction behaviour and contact stiffness due to repeated high-pressure contact and slip. *Tribol. Int.* **2022**, *170*, 107487. [CrossRef]
43. Piegl, L.; Tiller, W. *The NURBS Book*; Monographs in Visual Communication; Springer: Berlin/Heidelberg, Germany, 1997.
44. He, S.; Xuan, J.; Du, W.; Xia, Q.; Xiong, S.; Zhang, L.; Wang, Y.; Wu, J.; Tao, H.; Shi, T. Spiral tool path generation method in a nurbs parameter space for the ultra-precision diamond turning of freeform surfaces. *J. Manuf. Process.* **2020**, *60*, 340–355. [CrossRef]
45. Liu, T.; Gao, W.; Zhang, D.; Zhang, Y.; Chang, W.; Liang, C.; Tian, Y. Analytical modeling for thermal errors of motorized spindle unit. *Int. J. Mach. Tools Manuf.* **2017**, *112*, 53–70. [CrossRef]
46. Peng, C.; Peng, J.; Wang, Z.; Wang, Z.; Chen, J.; Xuan, J.; Shi, T. Adaptive fault diagnosis of railway vehicle on-board controller with large language models. *Appl. Soft Comput.* **2025**, *185*, 113919. [CrossRef]
47. Wang, Z.; Xuan, J.; Shi, T. Domain reinforcement feature adaptation methodology with correlation alignment for compound fault diagnosis of rolling bearing. *Expert Syst. Appl.* **2025**, *262*, 125594. [CrossRef]
48. Wang, Z.; Xuan, J.; Shi, T.; Li, Y.-F. Multi-label domain adversarial reinforcement learning for unsupervised compound fault recognition. *Reliab. Eng. Syst. Saf.* **2024**, *254*, 110638. [CrossRef]
49. Wang, Z.; Li, S.; Xuan, J.; Shi, T. Biologically inspired compound defect detection using a spiking neural network with continuous time-frequency gradients. *Adv. Eng. Inform.* **2025**, *65*, 103132. [CrossRef]

Disclaimer/Publisher's Note: The statements, opinions and data contained in all publications are solely those of the individual author(s) and contributor(s) and not of MDPI and/or the editor(s). MDPI and/or the editor(s) disclaim responsibility for any injury to people or property resulting from any ideas, methods, instructions or products referred to in the content.